

Synthesis, Crystal Structure, and Thermal Properties of the First Mixed-Metal and Anion-Substituted Rare Earth Borohydride $\text{LiCe}(\text{BH}_4)_3\text{Cl}$

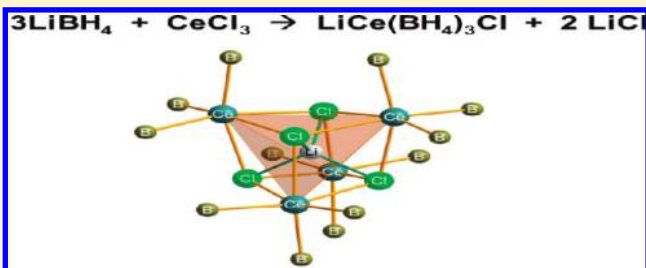
C. Frommen,^{*,†} M.H. Sørby,[†] P. Ravindran,[‡] P. Vajeeston,[‡] H. Fjellvåg,[‡] and B.C. Hauback[†]

[†]Institute for Energy Technology, Physics Department, P.O. Box 40, NO-2027 Kjeller, Norway

[‡]Center for Materials Science and Nano Technology, University of Oslo, P.O. Box 1033 Blindern, N-0315 Oslo, Norway

 Supporting Information

ABSTRACT: The mechanochemical reaction between LiBH_4 and CeCl_3 in a molar ratio of 3:1 has led to the formation of $\text{LiCe}(\text{BH}_4)_3\text{Cl}$. This compound is the first example of a mixed-metal and anion-substituted rare earth borohydride. The optimized structural parameters from total energy calculations based on DFT are in excellent agreement with the experimentally obtained data. The bonding interactions between constituents have been analyzed using charge density and partial density of states. The calculations suggest that $\text{LiCe}(\text{BH}_4)_3\text{Cl}$ is an insulator. $\text{LiCe}(\text{BH}_4)_3\text{Cl}$ crystallizes in the cubic space group $\bar{I}43m$ ($Z = 8$) with lattice constant $a = 11.5916(1)$ Å. It starts to decompose at ~ 220 °C and forms CeH_2 and amorphous boron containing species during dehydrogenation. The activation energy for the thermal decomposition was determined as 106(6) kJ/mol, and the material shows partial reversibility. Under 80 bar of hydrogen, 13% of the initial hydrogen content could be rehydrogenated at 340 °C.



INTRODUCTION

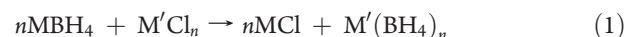
Borohydrides, also called tetrahydroborates, are a prospective class of materials for solid state hydrogen storage because of their high gravimetric hydrogen density of up to 20.8 wt % H for $\text{Be}(\text{BH}_4)_2$ and 18.5 wt % for LiBH_4 , respectively.^{1–3} They can be roughly divided into two main groups: (a) Materials that contain a metal ion with low electronegativity, like in the alkali metal borohydrides. This leads to an almost complete charge transfer from the metal to the BH_4 group, resulting in a predominant ionic character in the metal- BH_4 coordination. (b) Alkaline earth and transition-metal borohydrides that exhibit directionality, a higher electronegativity of the metal ion, and hence only partial charge transfer from the metal to the BH_4 group. The latter leads to a destabilization of the BH_4 unit by weakening of B–H bonds and results in lower decomposition temperatures of transition-metal borohydrides compared with alkali metal borohydrides.

Since the discovery of $\text{LiK}(\text{BH}_4)_2$ ⁴ and $\text{LiSc}(\text{BH}_4)_4$,^{5,6} the first crystalline mixed-metal (double cation) borohydrides, the combination of two metals with different electronegativity has been successfully used to tune the thermal stability of borohydrides. This in turn has made them more attractive as solid-state storage materials.

The mixed-metal borohydrides often exhibit structures and components that have no common analogue among other known inorganic compounds. The discrete complex $[\text{Sc}(\text{BH}_4)_4]^-$ anion has been observed for the first time in the series of $\text{MSc}(\text{BH}_4)_4$ ($\text{M} = \text{Li, Na, K}$) compounds.^{5–9} Similar complex anions like $[\text{Zn}(\text{BH}_4)_3]^-$

and $[\text{Zn}_2(\text{BH}_4)_5]^-$ were later also observed in the Zn-containing compounds $\text{MZn}(\text{BH}_4)_3$ and $\text{M}_2\text{Zn}(\text{BH}_4)_5$ ($\text{M} = \text{Li, Na}$).⁹ The structures of the Zn-series feature two doubly interpenetrated 3D frameworks similar to those found in metal organic frameworks (MOFs), and observed for the first time in a metal hydride.

Mechanochemistry, for example, ball-milling, has been successfully used to synthesize a variety of borohydrides, starting from a simple alkali borohydride and the corresponding metal chloride of the target material according to the metathesis reaction eq 1



Using the above approach, compounds like $\text{Mn}(\text{BH}_4)_2$,¹⁰ the first crystalline 3D-metal borohydride, and several rare earth borohydrides $\text{RE}(\text{BH}_4)_3$ ($\text{RE} = \text{Y, Dy, Gd}$)^{11–17} have been obtained recently. In addition, several bimetallic borohydrides were obtained via a more complex chemical reaction eq 2



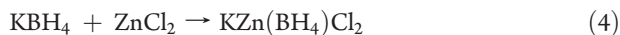
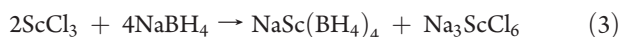
Among those are the series of Sc-containing $\text{MSc}(\text{BH}_4)_4$ ($\text{M} = \text{Li, Na, K}$) and Zn-containing compounds $\text{MZn}_2(\text{BH}_4)_5$ and $\text{MZn}(\text{BH}_4)_3$ ($\text{M} = \text{Li, Na}$).

Received: May 31, 2011

Revised: October 18, 2011

Published: October 18, 2011

In reality, the situation can be much more complex than that depicted by eqs 1 and 2 because the formation of ternary chlorides as well as that of mixed-cation and mixed-anion compounds are possible via addition reactions similar to eqs 3 and 4



$\text{KZn}(\text{BH}_4)\text{Cl}_2$ ¹⁸ and likewise $\text{NaY}(\text{BH}_4)_2\text{Cl}_2$ are two prominent examples of a new class of mixed-cation and mixed-anion compounds. The combination of different ligands in metal borohydrides seems to be a feasible way to adjust their stability with respect to thermal decomposition, for example, hydrogen release temperature.

Recently, two independent studies reported that ball-milling of LiBH_4 – CeCl_3 in a 3:1 molar ratio leads to the formation of cerium borohydride, $\text{Ce}(\text{BH}_4)_3$,^{19,20} with a cubic structure and lattice constant $a = 11.64$ Å. Because no further structural information was presented, however, we decided to repeat the synthesis procedure and to study the crystal structure of the product phase(s) by means of a combination of powder X-ray and neutron diffraction. To gain more insight into the structural stability and chemical bonding, additional *ab initio* calculations based on density functional theory (DFT) have also been performed.

In this Article, we present our findings and show that the product of this synthesis procedure is in fact $\text{LiCe}(\text{BH}_4)_3\text{Cl}$, the first mixed-cation mixed-anion rare earth borohydride.

EXPERIMENTAL SECTION

Sample Preparation. A mixture of $\text{Li}^{11}\text{BD}_4$ (>98%, Kat-Chem) or LiBH_4 (95% Sigma-Aldrich) and CeCl_3 (99.99% Sigma-Aldrich) in a molar ratio of 3:1 was milled in a Fritsch Pulverisette 6 Monomill at 500 rpm for 6 h (ball-to-powder ratio 60:1). In a typical experiment, 6.162 mmol CeCl_3 (1.519 g) and 18.486 mmol $\text{Li}^{11}\text{BD}_4$ (0.481 g) were used, resulting in a total powder mass of 2 g. Because of the strong neutron absorption of natural boron, the ^{11}B isotope was used in the synthesis. Furthermore, deuterium was selected because of lower incoherent scattering than the H-isotope. All sample handling and preparations were performed under an inert Ar atmosphere in an MBraun Unilab glovebox fitted with a recirculation system and gas/humidity sensors. Oxygen and water levels were kept below 1 ppm during all operations.

Initial Sample Characterization. All samples were initially investigated by powder X-ray diffraction (PXD) using a Bruker D8 Advance diffractometer (Cu – $\text{K}\alpha_{1,2}$ radiation) equipped with a 1D LynxEye detector. The samples were mounted in 0.5 mm diameter glass capillaries sealed with glue.

Powder Neutron Diffraction. Data at room temperature (RT) were collected with the PUS instrument²¹ at the JEEP II reactor at Kjeller, Norway. Neutrons with the wavelength $\lambda = 1.5557$ Å were obtained from a Ge (511) focusing monochromator. Data were collected from 10 to 130° in 2θ . The sample was contained in a rotating cylindrical vanadium sample holder with 6 mm diameter. The vanadium sample holder was closed with an indium wire O-ring in the glovebox before the data collection to avoid oxidation.

Structure solution was performed by *ab initio* methods with the FOX program.^{22,23} Rietveld refinement was carried out using

the FULLPROF program.²⁴ The background for both data sets was modeled by linear extrapolation between 15 manually chosen points. The Thompson–Cox–Hastings pseudo-Voigt profile function was selected for the global refinement of the PXD and powder neutron diffraction (PND) data sets. Unit cell parameters, zero-point, overall scale factors, peak shape mixing parameters, three Gaussian profile parameters (UVW), and two Lorentzian profile parameters were refined for each data set.

Differential Scanning Calorimetry (DSC). Measurements were performed with a SensysDSC from SETARAM. Samples were placed either inside aluminum crucibles and sealed with pierced lids made of the same material or in airtight, high-pressure capable containers made of stainless steel ($p_{\text{max}} = 500$ bar; $T_{\text{max}} = 600$ °C). The data were collected under flowing argon (15 mL/min) using a constant heating rate of 2 °C/min.

Simultaneous Thermogravimetric Analysis (TGA) with DSC. Experiments were performed with a Netzsch STA 449 F3 Jupiter instrument. Samples were measured in Al_2O_3 sample pans equipped with pierced lids made of the same material. The material was heated between 30 and 600 °C with a constant rate of 2 °C/min under argon gas (50 mL/min). The measurements were baseline corrected by means of the Proteus software package.

Synchrotron Radiation Powder X-ray Diffraction (SR-PXD). Time-resolved data were collected at the Swiss-Norwegian beamline (SNBL), station BM01A, at the European Synchrotron Radiation Facility (ESRF) in Grenoble, France. The samples were mounted in 0.5 mm boron–silica–glass capillaries, kept in place by a glass rod and mounted in a Swagelok fitting. The capillary was then evacuated with a rotary pump and kept under dynamic vacuum. Two-dimensional powder data were collected using an imaging plate system (MAR345) with an exposure time of 30 s. The capillaries were rotated 30° during the exposure to reduce texture effects. For data readout and erasing, 90 s was needed, and thus complete data sets were collected every second minute. The wavelength was 0.70947 Å. The 2D data were integrated to yield 1D powder diffraction patterns with the program FIT2D²⁵ and binned with a step size of 0.016°.

High-resolution (HR) SR-PXD measurements were performed at SNBL, station BM01B, with a wavelength of 0.50123 Å between $2\theta = 2$ and 25° with a step-size of 0.003° (2θ) and binned at 0.006°.

Temperature-Programmed Desorption (TPD) and Residual Gas Analysis (RGA). TPD and RGA were measured in an in-house-developed setup under vacuum (10^{-5} mbar) between RT and 600 °C with a constant heating rate of 2 °C/min. RGA was measured with a MULTIVISON IP detector system coupled to a PROCESS Eye analysis package from MKS Instruments.

Infrared Spectroscopy. Infrared spectroscopy was carried out on a BRUKER IFS 66v spectrometer equipped with a DTGS detector. The powders were embedded in KBr pellets (7 mm) with a 0.5% mass concentration. The transmission spectra of the KBr pellets were recorded in the 400–8000 cm^{-1} region with a resolution of 4 cm^{-1} . Scattering contribution to the spectra due to the presence of KBr is considered to be negligible in this region.

Computational Methodology. First principles DFT calculations were performed using the Vienna *ab initio* simulation package (VASP)²⁶ within the projector-augmented wave (PAW) method²⁷ as implemented by Kresse and Joubert.²⁸ The Kohn–Sham equations²⁹ were solved self-consistently using an iterative matrix diagonalization method. This is based on a band-by-band preconditioned conjugate gradient³⁰ method with an improved

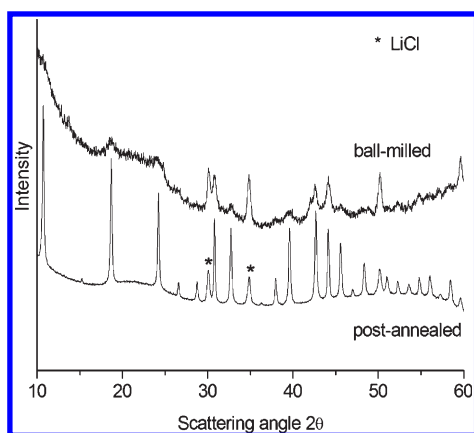


Figure 1. PXD pattern for a mixture of $\text{LiBD}_4\text{-CeCl}_3$ (3:1 ratio) after ball-milling and after postannealing at 165 °C and 60 bar of deuterium.

Pulay mixing³¹ to obtain efficiently the ground-state electronic structure. The forces on the atoms were calculated using the Hellmann–Feynman theorem, and they are used to perform a conjugate gradient relaxation. Structural optimizations were continued until the forces on the atoms had converged to <1 meV/Å and the pressure on the cell had minimized within the constraint of constant volume. The calculations were performed within periodic boundary conditions allowing the expansion of the crystal wave functions in terms of a plane-wave basis set.

Among the LDA and GGA functionals, the PBESol GGA functional^{32,33} generally gives good equilibrium structural parameters and hence we have used PBESol functional for the present calculation. Ground-state geometries were determined by minimizing stresses and Hellman–Feynman forces using the conjugate-gradient algorithm with force convergence $<10^{-3}$ eV Å⁻¹. Brillouin zone integration was performed with a Gaussian broadening of 0.1 eV during all relaxations. From various sets of calculations, it was found that the $4 \times 4 \times 4$ k point set with a 500 eV plane-wave cutoff is sufficient to ensure optimum accuracy in the computed results. All Brillouin zone integrations were performed on Γ -centered symmetry-reduced Monkhorst-Pack k-point meshes using the tetrahedron method with Blöchl corrections.³⁴ We have not considered the spin-polarization into the calculation because the magnetic interactions will originate from the well-localized 4f electrons in the Ce^{3+} ions, and hence it will only have minor influence on the structural properties.

RESULTS AND DISCUSSION

The PXD pattern of the ball-milled mixture shows that the peaks associated with the starting materials CeCl_3 and LiBD_4 have disappeared and that a metathesis reaction has occurred. New peaks associated with the title compound and LiCl have developed instead (Figure 1). Because the peaks of the product phases were very broad and weak, a postannealing procedure was undertaken. The powder mixture was heated in a Sieverts-type apparatus with a heating rate of 9 °C/min for 24 h under deuterium backpressure of 60 bar and temperatures up to 165 °C. The resulting PXD pattern in Figure 1 (bottom) now shows the product phases in a highly crystalline state. Indexing with the program DICVOL06³⁵ resulted in a cubic unit cell with lattice parameter $a = 11.595(1)$ Å. Further inspection of the hkl indices showed special selection based on $(h + k + l) = 2n$, indicating the presence of a body-centered unit cell. Analysis of

possible space groups with CHEKCELL³⁶ gave $\bar{I}43m$ as the most probable candidate. The PXD pattern of the postannealed mixture resembles the data presented by Gennari et al., who assigned their product to $\text{Ce}(\text{BH}_4)_3$ (cubic, $a = 11.64$ Å).

On the basis of HR SR-PXD and PND data sets of the doubly labeled (^2H , ^{11}B) material, structure solution with ab initio methods was attempted. The FOX program was used to create a model in space group $\bar{I}43m$ based initially on the assumption that the product was $\text{Ce}(\text{BH}_4)_3$. Large differences between the assumed model and the experimental data were observed, especially for the strongest peaks in the PXD data but also in the PND diagram. As a second step, further (BD_4) units were added, which proved to be unsuccessful as well. In the next step, a single chlorine atom was added to the model, which resulted in a significant improvement for both PXD and PND data sets. Because Cl has the highest neutron cross section of all the elements present in the mixture (Li, Ce, ^{11}B , ^2H , Cl), its presence will influence the intensities of the peaks in the PND pattern significantly. Ce is dominating in the PXD pattern but has the smallest neutron cross section. The combined model resulted in cerium and chlorine, both taking (8c) positions, with atomic coordinates (0.855 0.855 0.855) and (0.891 0.109 0.891), respectively, and boron adopting a (24g) position (0.134 0.622 0.622) with three surrounding D atoms: two in (24g) and one in (48h). The model was completed by compensating the excess negative charge of the $[\text{Ce}(\text{BD}_4)_3\text{Cl}]^-$ unit with 2 lithium atoms: one in the (6b) position (0 1/2 1/2) and the other in the (2a) position (0 0 0) resulting in the overall composition of $\text{LiCe}(\text{BD}_4)_3\text{Cl}$.

A combined Rietveld refinement on the structure model was carried out with the FULLPROF program. The fit after convergence is shown in Figure 2, and crystallographic data including interatomic distances and angles are presented in Tables 1 and 2. The optimized structural parameters from total energy calculations based on DFT have been included for comparison. The calculated unit cell dimensions and positional parameters at 0 K and ambient pressure are in good agreement with the experimental values obtained at RT (Table 1).

For Rietveld refinement, the HR SR-PXD and PND powder patterns were weighted as 1:9. Initially, the position of the cerium atom was kept fixed and later relaxed once the refinement was close to convergence. Isotropic displacement parameters, B_{iso} , were refined groupwise, and no constraints were used on bond distances and angles, thus allowing free refinement of all atomic coordinates. This resulted in the following reliability factors: $R_p = 6.30$, $R_{\text{wp}} = 8.19$, and $\chi^2 = 2.75$ for the HR SR-PXD pattern, and $R_p = 3.37$, $R_{\text{wp}} = 4.29$, and $\chi^2 = 1.74$ for the PND data set. Weight fractions were obtained as follows: $\text{LiCe}(\text{BD}_4)_3\text{Cl}$: 75.7(6)%, LiCl : 24.3(4)% for the HR SR-PXD pattern, and $\text{LiCe}(\text{BD}_4)_3\text{Cl}$: 77(1)%, LiCl : 22.9(3)% for the PND pattern. The weight contribution of the cerium containing material is slightly less in the PXD case and is probably caused by X-ray absorption.

Taking into account the overall reaction scheme



the experimentally determined weight fractions are in excellent agreement with the calculated ones for $\text{LiCe}(\text{BD}_4)_3\text{Cl}$ and LiCl , which are 73.8 and 26.2%, respectively.

Crystal Structure of $\text{LiCe}(\text{BD}_4)_3\text{Cl}$. The title compound crystallizes in the cubic space group $\bar{I}43m$ ($Z = 8$) with the lattice constant $a = 11.5916(1)$ Å. Figure 3a shows a representation of

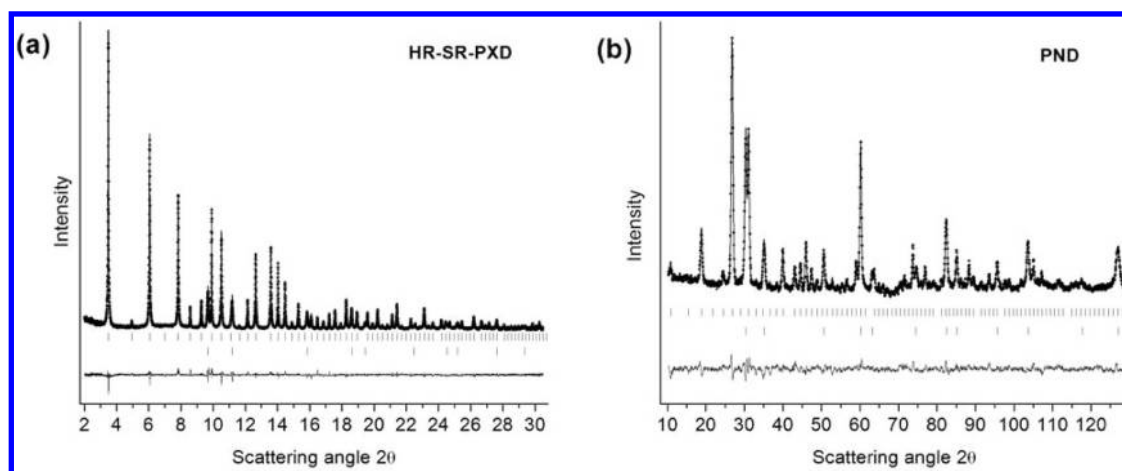


Figure 2. Final fits after convergence for a combined refinement using high-resolution synchrotron data (a) and powder neutron diffraction data (b). Peak positions for LiCe(BD₄)₃Cl (top) and LiCl (bottom) have been indicated by tick marks.

Table 1. Crystallographic Data for LiCe(BD₄)₃Cl Obtained from Experimental Data and Theoretical Structural Optimization by DFT

phase data					
formula sum	Ce ₁ B ₃ D ₁₂ Cl ₁ Li ₁				
formula weight	239.11 g/mol				
crystal system	cubic				
space group	I $\bar{4}3m$ (217)				
cell parameters	$a = 11.5917(1)$ Å $a = 11.665$ Å (theory)				
cell volume	$1557.54(5)$ Å ³				
Z	8				
calcd density	2.03926 g/cm ³				
atom	Wyckoff position	x/a	y/b	z/c	Biso [Å ²]
Ce1	8c	0.8576(7)	0.8576(7)	0.8576(7)	1.27(2)
theory		0.8484	0.8484	0.8484	
B	24g	0.1295(9)	0.6237(8)	0.6237(8)	1.34(2)
theory		0.1305	0.6208	0.6208	
D1	24g	0.0273(15)	0.6163(12)	0.6163(12)	7.68(2)
theory		0.0267	0.6142	0.6142	
D2	48h	0.1747(8)	0.6417(14)	0.5357(11)	7.68(2)
theory		0.1759	0.6519	0.5297	
D3	24g	0.1548(13)	0.6888(12)	0.6888(12)	7.68(2)
theory		0.1527	0.6945	0.6945	
Cl	8c	0.8902(8)	0.1098(8)	0.8902(8)	1.02(2)
theory		0.8927	0.1073	0.8927	
Li1	6b	0	1/2	1/2	1.30(2)
theory		0	1/2	1/2	
Li2	2a	0	0	0	1.30(2)
theory		0	0	0	

the unit cell content and Figure 3b–d highlights the local coordination around the cerium atom and the two crystallographic-independent lithium atoms. Cerium is octahedrally coordinated by three [BD₄][−] groups with Ce–B distances of 2.662(11) Å and three chlorine atoms with Ce–Cl bond distances of 2.972(7) Å

Table 2. Selected Interatomic Distances and Angles for LiCe(BD₄)₃Cl Obtained from a Combined Refinement Using PND/PXD Data and from Structural Optimization Using DFT Calculations

atom 1	atom 2	count	experiment	theory
			d [Å]	d [Å]
Ce1	D2	6x	2.454(15)	2.477(6)
	D3	3x	2.471(15)	2.496(6)
	B1	3x	2.662(11)	2.610(5)
	Li2	1x	2.859(8)	2.858(1)
B1	Cl1	3x	2.972(7)	2.966(3)
	D3	1x	1.107(17)	1.152(7)
	D2	2x	1.166(18)	1.154(8)
	D1	1x	1.191(21)	1.215(7)
Li1	D1	4x	1.933(14)	1.918(7)
	B1	4x	2.523(10)	2.540(5)
	D2	8x	2.640(13)	2.669(6)
Li2	Cl1	4x	2.204(10)	2.193(2)
	Ce1	4x	2.859(8)	2.858(1)
atom 1	atom 2	atom 3	angle [deg]	
B1	D3	D2	110.7(1)	
	D3	D2	110.7(1)	
	D3	D1	111.4(1)	
	D2	D2	95.4(1)	
	D2	D1	113.8(1)	
	D2	D1	113.8(1)	

forming a CeB₃Cl₃ octahedron. Furthermore, each chlorine atom acts as a η^3 -ligand and shares bridges with three neighboring CeB₃Cl₃ octahedra resulting in the formation of a Ce₄–Cl₄ tetrameric unit that takes up the shape of a distorted heterocubane (Figure 3c). In contrast with the chlorine atoms, the [BD₄][−] units are all terminal and do not engage into bridging (Figure 3c). The Ce–Cl bond length of 2.972(7) Å in the tetramer is considerably longer than those found in the corner-connected elpasolites Cs₂NaCeCl₆ (2.82 Å)³⁷ or Cs₃CeCl₆ (2.711 Å)³⁸ and somewhat longer than for typical edge-sharing

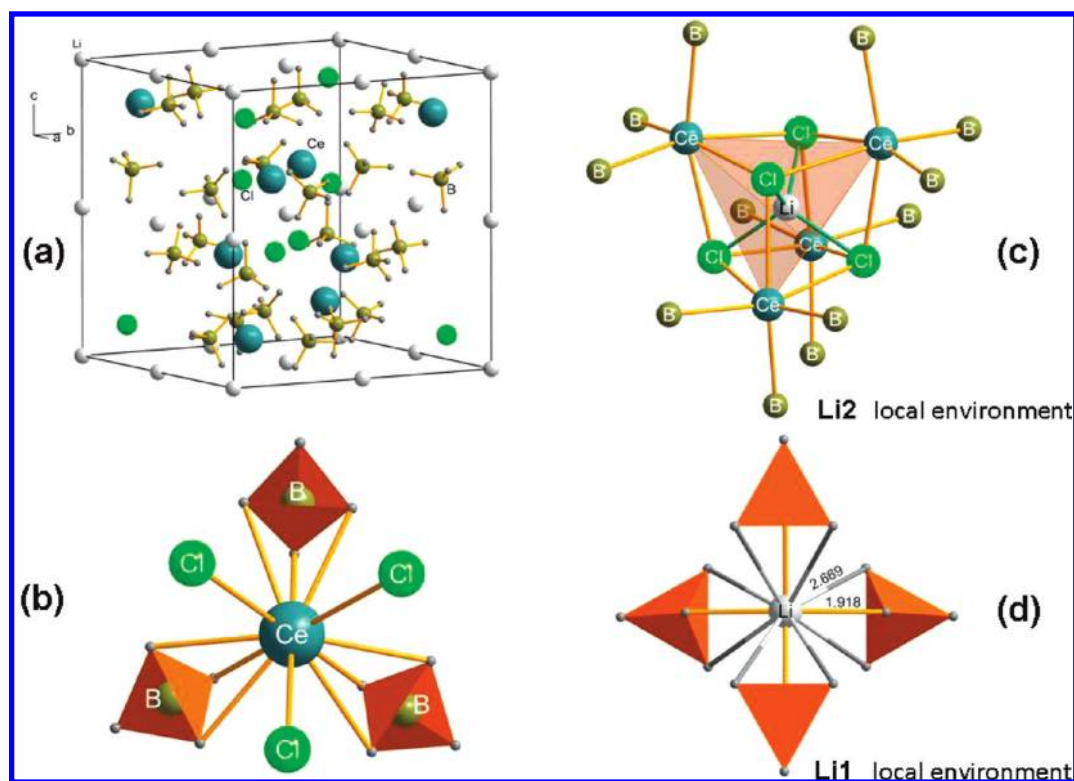


Figure 3. (a) Unit cell content for $\text{LiCe}(\text{BD}_4)_3\text{Cl}$. (b) Local coordination around the central Ce^{3+} cation. (c,d) Local coordination for the two independent lithium positions in the structure of $\text{LiCe}(\text{BD}_4)_3\text{Cl}$.

dimers like $\text{Ce}_2\text{Cl}_6(\text{CH}_3\text{OH})_8$ (2.8517 to 2.9223 Å) and $\text{Ce}_2\text{Cl}_6(\text{DMF})_4$ (2.884 to 2.927 Å).³⁹ However, such a long Ce–Cl bond length has been observed for CeCl_3 , which is built from edge- and face-connected CeCl_6 octahedra with Ce–Cl bond distances ranging from 2.9588 to 2.9662 Å.⁴⁰

To the best of our knowledge, this is the first report of a purely inorganic lanthanide containing tetramer and is therefore unique in its own sense. Such structures are typically found only in conjunction with organic linkers, for example, in tetrameric lanthanide neopentoxide complexes or in some lanthanide alkoxides like samarium isopropoxide.

In addition to the three chlorine ligands, the central Ce^{3+} cation is surrounded by three $[\text{BD}_4]^-$ groups. The coordination to the metal is realized via triangular faces resulting in an overall coordination number (CN) of $9\text{H} + 3\text{B} + 3\text{Cl} = 15$ (Figure 3b). The Ce–H bond distances range from 2.45(1) to 2.47(1) Å and are somewhat larger than those found in $\text{Y}(\text{BH}_4)_3$ (2.229 to 2.357 Å).¹² This increase is mainly due to the difference in effective ionic radii for Y^{3+} and Ce^{3+} , which are 90 and 101 pm, respectively.⁴¹

In addition to the crystallographic studies, IR and Raman experiments were performed on $\text{LiCe}(\text{BD}_4)_3\text{Cl}$ as well as on the starting material $\text{Li}^{11}\text{BD}_4$. The initial IR experiments on $\text{Li}^{11}\text{BD}_4$ in KBr pellets displayed major B–D stretching frequencies at 1749, 1716, 1675, and 1628 cm^{-1} respectively (not shown). Compared with the vibrational frequencies obtained by Harvey and McQuaker⁴² at 80 K, which are 1736, 1722, and 1606 cm^{-1} , respectively, one notes a significant difference. One possible explanation for this could be the partial formation of KBD_4 in KBr, which cannot be excluded a priori. Furthermore, the presence of water in the sample was confirmed by the

appearance of a broad maximum around 3500 cm^{-1} . To minimize the risk of hydrolysis and ion exchange in the pellets, the KBr was therefore carefully dried under vacuum at a temperature of 250 °C, and the spectra of $\text{LiCe}(\text{BD}_4)_3\text{Cl}$ were recorded immediately after the pellet had been pressed. The result is presented in the top part of Figure 4a, which displays the IR spectrum of $\text{LiCe}(\text{BD}_4)_3\text{Cl}$ in the spectral range of 400–4000 cm^{-1} . The IR spectrum shows two characteristic regions: the first is associated with the internal B–D bending modes (700–1000 cm^{-1}), and the second corresponds to the internal B–D stretching modes (1500–1900 cm^{-1}). Those regions have been highlighted by rectangles and indicated by text markers. In addition, there are multiple weak bands visible between 2100 and 2500 cm^{-1} that correspond to B–H stretching vibrations. They result in part from the fact that the $\text{Li}^{11}\text{BD}_4$ starting material was not isotopic pure but contained residual hydrogen. A second reason for their appearance could be residual moisture coupled to partial H–D exchange. The fact that the characteristic –OH stretching vibration around 3500 cm^{-1} is not visible, however, makes the first assumption more likely.

To exclude possible exchange reactions and hydrolysis, complementary Raman experiments on $\text{LiCe}(\text{BD}_4)_3\text{Cl}$ were performed with a laser wavelength of 532 nm in sealed glass capillaries, and the result is presented in Figure 4a (bottom). In addition, Figure 4b–e displays the B–D bending and stretching regions for $\text{Li}^{11}\text{BD}_4$ and $\text{LiCe}(\text{BD}_4)_3\text{Cl}$ in more detail, with spectra being deconvoluted by a series of Lorentzians. The measured frequencies for $\text{Li}^{11}\text{BD}_4$ in the B–D bending region are: $\nu_4 = 834$, $\nu_{2'} = 925$, and $\nu_2 = 948$ cm^{-1} , respectively (Figure 4b) and are in excellent agreement with published results for LiBD_4 by Racu et al.⁴³ The major frequencies for $\text{Li}^{11}\text{BD}_4$ in

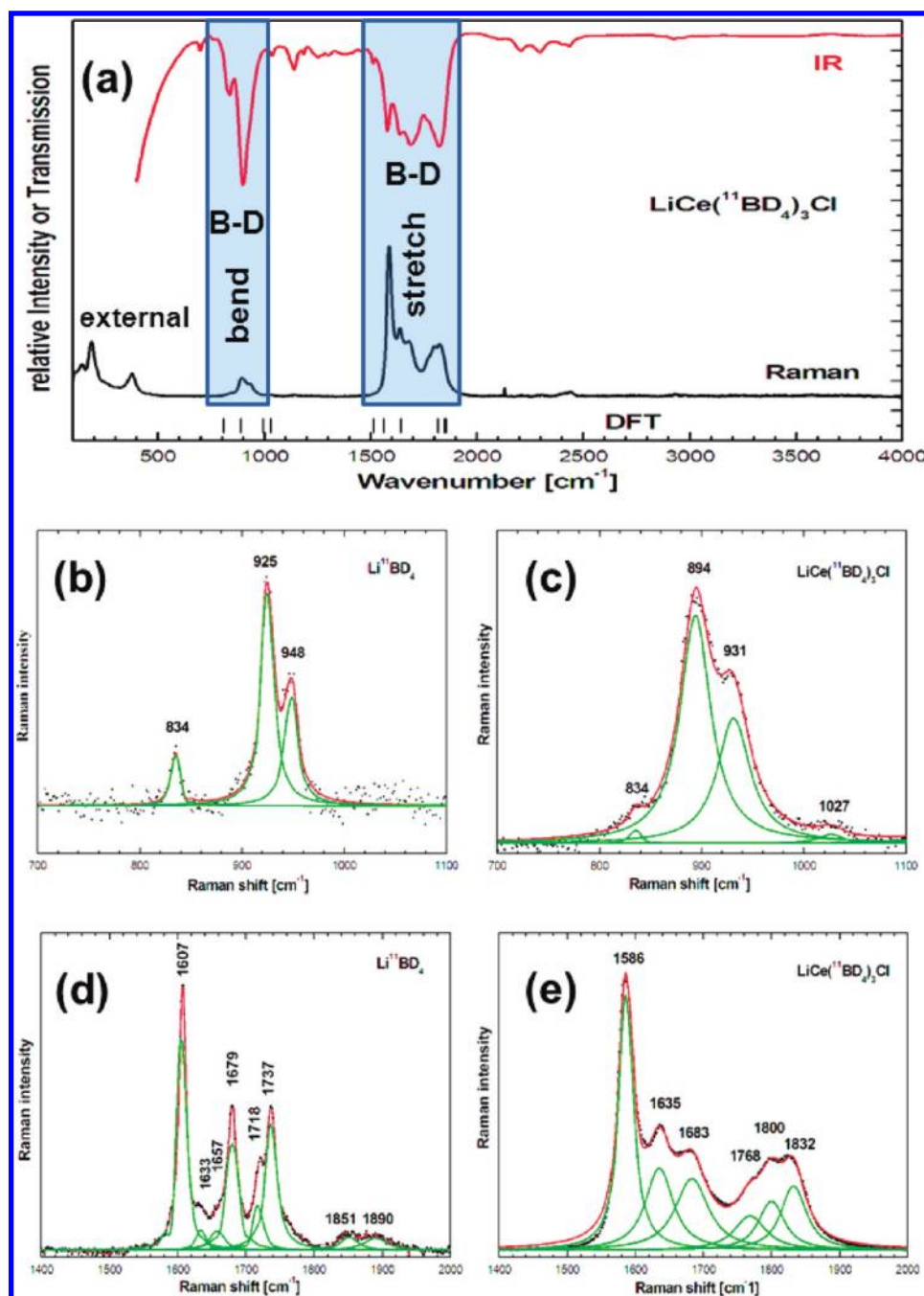


Figure 4. (a) Full-scale IR and Raman spectra for LiBD_4 and $\text{LiCe}(\text{BD}_4)_3\text{Cl}$ and calculated IR and Raman active frequency modes for the B-D bending and stretching region. (b–e) Raman spectra for LiBD_4 and $\text{LiCe}(\text{BD}_4)_3\text{Cl}$ with emphasis on the B-D bending and stretching regions. The spectra have been deconvoluted by a series of Lorentzians.

the stretching region (Figure 4d) are: $\nu_1 = 1607$, $\nu_3 = 1679$, $\nu_{3'} = 1718$, and $\nu_{3''} = 1737$ cm^{-1} . In addition weak bands at $2\nu_2 = 1851$ and $2\nu_2 = 1890$ cm^{-1} appear as well as weak bands at $2\nu_4 = 1657$ and possibly $^{10}\text{B}\nu_1 = 1633$ cm^{-1} .

The Raman spectrum for $\text{LiCe}(^{11}\text{BD}_4)_3\text{Cl}$ in the bending region (Figure 4c) shows similarities to that of LiBD_4 . A doublet with major frequencies is found at 894 and 931 cm^{-1} together with shoulders of weak intensity at 834 and 1027 cm^{-1} , respectively. The major frequencies are shifted toward lower wavenumbers compared with LiBD_4 , and their separation has increased from 23 to 37 cm^{-1} . This increased separation could

hint toward a more distorted coordination and differences in bond lengths, and the shift in frequencies toward lower wavenumbers can be attributed to a decrease in electronegativity of the central cation due to the presence of Cerium. The stretching vibrations of $\text{LiCe}(^{11}\text{BD}_4)_3\text{Cl}$ presented in Figure 4e are also quite similar to those found for LiBD_4 . There is a group of three intense bands at 1586, 1635, and 1683 cm^{-1} , respectively, and their position is shifted to lower wavenumbers compared with those observed for LiBD_4 . In addition, a group of three medium to low intensity bands appear at 1768, 1800, and 1832 cm^{-1} . They could result from a combination of bands from the B-D

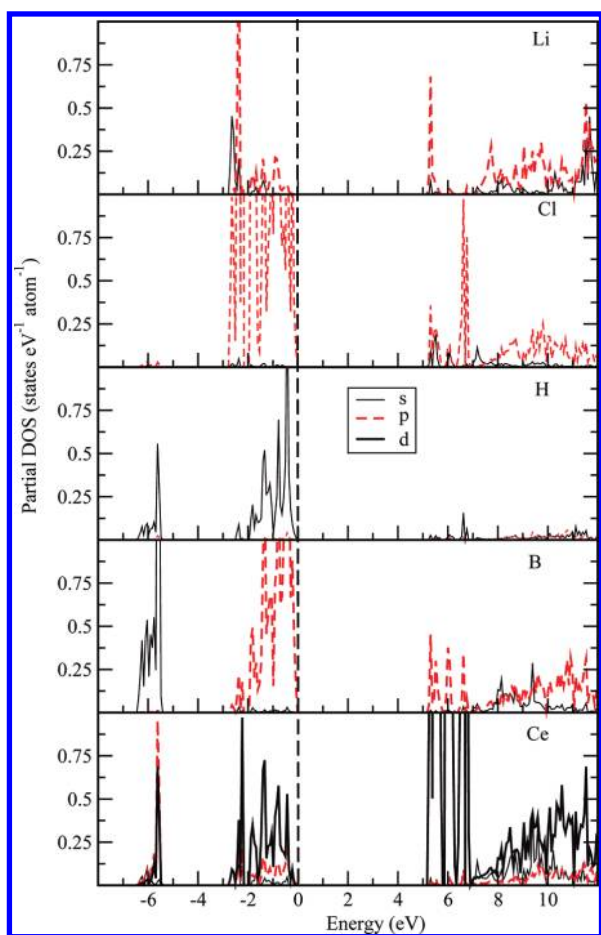


Figure 5. Partial density of states for $\text{LiCe}(\text{BH}_4)_3\text{Cl}$ after structural optimization. The Fermi level is set to zero.

bending region, for example, $(894 + 894) \rightarrow 1788 \text{ cm}^{-1}$, which is close to the observed 1800 cm^{-1} , as well as $(894 + 931) \rightarrow 1825 \text{ cm}^{-1}$, which is close to the observed band at 1832 cm^{-1} . The combination of different local environments and different central cations coupled to the $[\text{BD}_4]$ tetrahedra makes an assignment of those bands rather speculative, however, and is furthermore beyond the scope of this work.

The Raman- and IR-mode frequencies for the $\text{LiCe}(\text{BD}_4)_3\text{Cl}$ phase have also been obtained from DFT by using the finite displacement method as implemented in the CASTEP package.⁴⁴ In this method, a specific atom is displaced to induce the forces to act on the surrounding atoms, which are calculated via the Hellmann–Feynman theorem. The forces were collected to construct the force-constant matrices. The dynamical matrices were then solved to obtain phonon frequencies. For the CASTEP computation, the optimized crystal structure obtained from VASP calculations with a similar k -point mesh has been used as input with norm-conserving pseudopotentials (energy cutoff 700 eV) and the GGA exchange correlation functional proposed by PBE. Full geometry optimization was made again to check the reliability of CASTEP calculations, and it was found that the equilibrium lattice parameters and atomic positions obtained from both codes are almost the same. The calculated Raman frequencies for the B–D bending and stretching regions have been added as a stick plot on the bottom of Figure 4a. The calculated mode frequencies are in good agreement with the

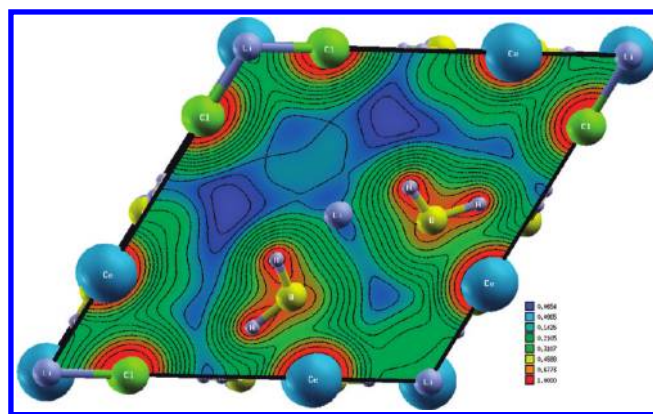


Figure 6. Calculated charge density plot for $\text{LiCe}(\text{BH}_4)_3\text{Cl}$.

experimentally obtained Raman frequencies. A full list of all Raman and IR active modes can be found in the Supporting Information.

Electronic Structure and Chemical Bonding. To understand the bonding interaction between the constituents, we have calculated the partial density of states (PDOS), as shown in Figure 5. The calculations show that this material is an insulator with a band gap value of 5.12 eV. The Ce atom donates its valence electrons to the host lattice, and hence negligibly small s -states of Ce are present in the valence band. Li also donates almost all of its $2s$ valence electrons to the Cl site, and hence the valence band DOS from the Li atom is very small. In contrast, there is a large valence band DOS present at the Cl site, indicating that the bonding interaction between Li and Cl is dominantly ionic.

In general, in borohydrides the strongest bonding interaction is between boron and hydrogen. So, if one intends to reduce the hydrogen desorption temperature, then one should weaken the B–H bonds. Hence, it is interesting to investigate the bonding interaction between boron and hydrogen in $\text{LiCe}(\text{BH}_4)_3\text{Cl}$. If the bonding interaction between B and H were purely ionic, then the valence band DOS at the B site would be completely empty. However, the partial DOS curves shown in Figure 5 clearly demonstrate that there is a finite s electron DOS present around -6 eV below the valence band maximum (VBM). In addition, there is a large amount of $2p$ electrons DOS present between -3 eV and VBM, clearly indicating that the B $2s$ and $2p$ electrons are not fully transferred to H. The s electron states at the H sites are energetically dispersed with the p states of B. Also, both hydrogen and boron atoms are spatially present adjacent to each other in the $\text{LiCe}(\text{BH}_4)_3\text{Cl}$ lattice, indicating that the bonding interaction between B and H possesses finite covalent character.

To gain more insight into the bonding interaction between constituents, we have performed charge density analysis of $\text{LiCe}(\text{BH}_4)_3\text{Cl}$, as shown in Figure 6. From this Figure, it is clear that a negligible amount of electrons is present at the Li site and hence the Li ions completely donate their electrons to the host lattice. There is a finite amount of electrons present at the Cl site. Those electrons are spherically distributed around the nucleus, indicating ionic interaction. As we have included semicore $5p$ states of Ce into our calculation, there are finite electrons present at the Ce site. However, the charge density distribution at the Ce site is spherically symmetric (Figure 6), and thus the bonding interaction between Ce and the host lattice also has dominant ionic character.

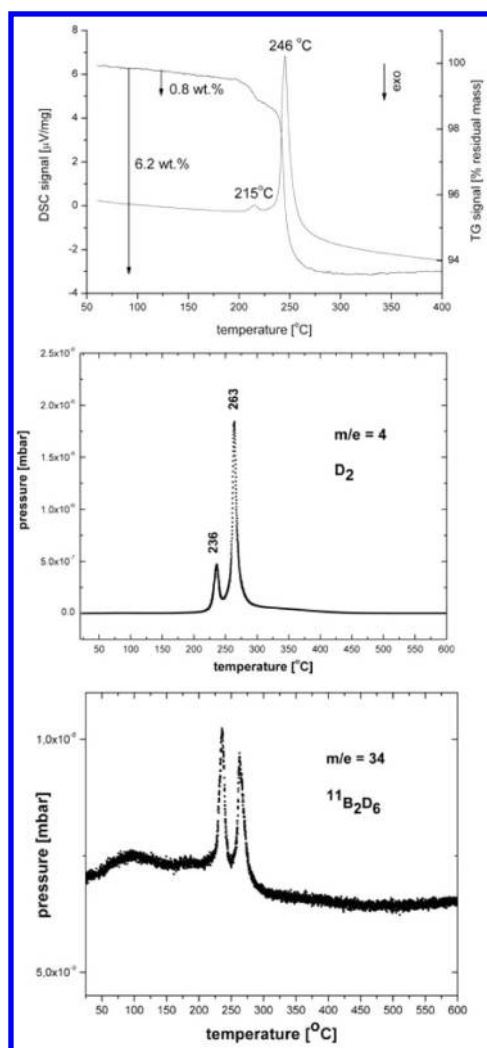


Figure 7. (top) Simultaneous TG-DSC for a ball-milled mixture of $\text{LiBD}_4\text{-CeCl}_3$ in a 3:1 ratio. (middle) Partial pressures for D_2 and (bottom) partial pressure for B_2D_6 obtained from RGA in the temperature range between 30 and 600 °C.

The charge density analysis shows the presence of molecular-like BH_4 structural subunits with finite charge density distribution in between B and H. This charge distribution is directional-dependent; in particular, the charge density at the H sites is polarized toward B. Therefore, the charge density analysis confirms the presence of finite covalent bonding between boron and hydrogen, consistent with the conclusion arrived from our partial DOS analysis. However, the amount of electrons at the B sites is much smaller than that in the neutral B atom, indicating the electron donation from B to the H atoms. It can therefore be concluded that the bonding interaction between B and H in $\text{LiCe}(\text{BH}_4)_3\text{Cl}$ has mixed ionic-covalent character.

It is interesting to know why $\text{LiCe}(\text{BH}_4)_3\text{Cl}$ is stabilized instead of $\text{Ce}(\text{BH}_4)_3$ in the mechanochemical reaction between LiBH_4 and CeCl_3 . The present charge density analysis shows that there is finite nonspherical charge density distributed between Cl and Ce as well as between the Cl atoms in the $\text{LiCe}(\text{BH}_4)_3\text{Cl}$ lattice. This could bring extra contributions to the structural stability compared with that in $\text{Ce}(\text{BH}_4)_3$.

Thermal Decomposition of $\text{LiCe}(\text{BD}_4)_3\text{Cl}$. The thermal decomposition of $\text{LiCe}(\text{BD}_4)_3\text{Cl}$ obtained by ball-milling of a

$\text{LiBD}_4\text{-CeCl}_3$ mixture in a 3:1 molar ratio was studied by means of simultaneous TG and DSC experiments. In addition, the nature of the evolved gases was followed in situ by means of RGA.

The TG-DSC traces in Figure 7 (top) were obtained by heating the material at a constant rate of 2 °C/min under Argon flow (50 mL/min) in an Al_2O_3 sample pan equipped with a pierced lid made of the same material. The DSC curve shows no signals for the orthorhombic–hexagonal phase transition (110 °C) and melting (285 °C) of LiBD_4 , indicating that all of the starting material has been converted during the mechanical milling process. A weak and broad endothermic peak in the DSC at 215 °C is accompanied by a mass loss of 0.8 wt %. A second major endothermic peak at 246 °C is coupled to a mass loss of 5.4 wt %. The accumulated mass loss between RT and 400 °C is ~6.2 wt % with respect to the total mass of the ball-milled mixture.

The RGA shows two distinct gas release events at 236 and 263 °C, respectively, with the majority of the gas being released in the second step. This is in agreement with the TG-DSC results, where the endothermic event at lower temperatures was only accompanied by a minor gas loss. The higher gas-release temperatures compared with the TG-DSC experiment are mainly due to different positions of the respective thermometers, which in the case of the RGA apparatus was situated close to the oven, unlike the TG-DSC setup, where the temperature is measured at the sample. For the RGA, the partial pressure of several species like deuterium ($m/e = 4$), diborane, B_2D_6 , ($m/e = 34$), and its fragments B_2D_5 , B_2D_4 , and BD_3 with $m/e = 32$, 30, and 17, respectively, was recorded during the desorption process. The signal for deuterium was the strongest by far and resulted in a maximum partial pressure of $\sim 2 \times 10^{-6}$ mbar at the peak temperature of 263 °C (Figure 7, middle). The partial pressure of diborane, on the other hand, only reached $\sim 1 \times 10^{-8}$ mbar during the desorption process (Figure 7, bottom). This indicates that the thermal decomposition of the $3\text{LiBD}_4\text{-CeCl}_3$ mixture proceeds almost exclusively by release of deuterium and that boron is kept in the solid state. This is one of the prerequisites for reversible hydrogen storage in borohydrides.

The decomposition temperature of the material is drastically reduced compared with that of neat LiBD_4 , which can be as high as 400 °C. The addition of CeCl_3 results in a destabilization of LiBD_4 , caused by the formation of the mixed-metal and anion substituted borohydride, $\text{LiCe}(\text{BD}_4)_3\text{Cl}$. This compound has two metal ions with different electronegativity, and the reduction in desorption temperature compared with LiBD_4 is probably caused by the presence of the more electronegative element cerium, which weakens B–H bonds.⁴⁵

A similar destabilization effect was recently observed in ball-milled mixtures of LiBH_4 with the halides CeX_3 and LaX_3 ($\text{X} = \text{Cl}, \text{F}$), for which decomposition temperatures in the range of 220–320 °C were obtained.²⁰ The most significant decrease in temperature was found for mixtures containing either CeCl_3 or LaCl_3 , but this was attributed to the formation of $\text{Ce}(\text{BH}_4)_3$ and $\text{La}(\text{BH}_4)_3$, respectively, instead of the formation of the mixed metal borohydride, $\text{LiCe}(\text{BD}_4)_3\text{Cl}$, which was observed in the present study.

The desorption kinetics of the $3\text{LiBD}_4\text{-CeCl}_3$ mixture after ball-milling for 6 h was studied also by means of DSC using different heating rates between 2 and 25 °C/min. Figure 8a shows that the decomposition is a multistep process with possibly three individual steps, as can be seen from the DSC trace obtained for the heating rate of 25 °C/min. In this case, two

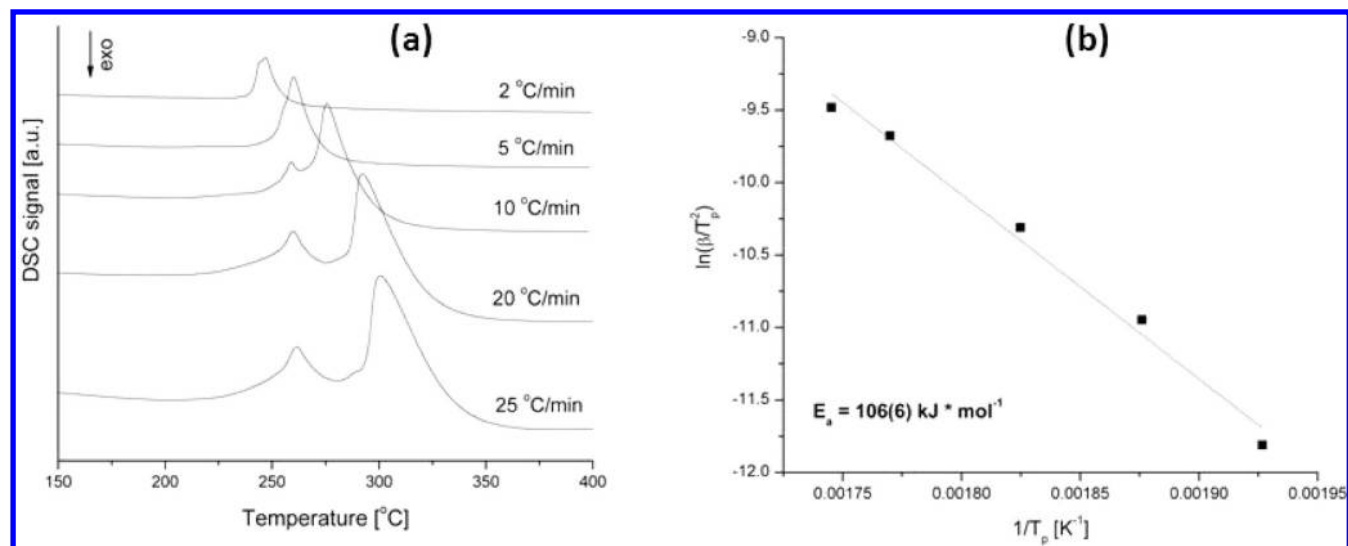


Figure 8. (a) DSC curves for $\text{LiBD}_4\text{-CeCl}_3$ (3:1) after 6 h of ball-milling using different heating rates. (b) Kissinger plot of the thermal desorption curves obtained for heating rates between 2 and 25 °C/min.

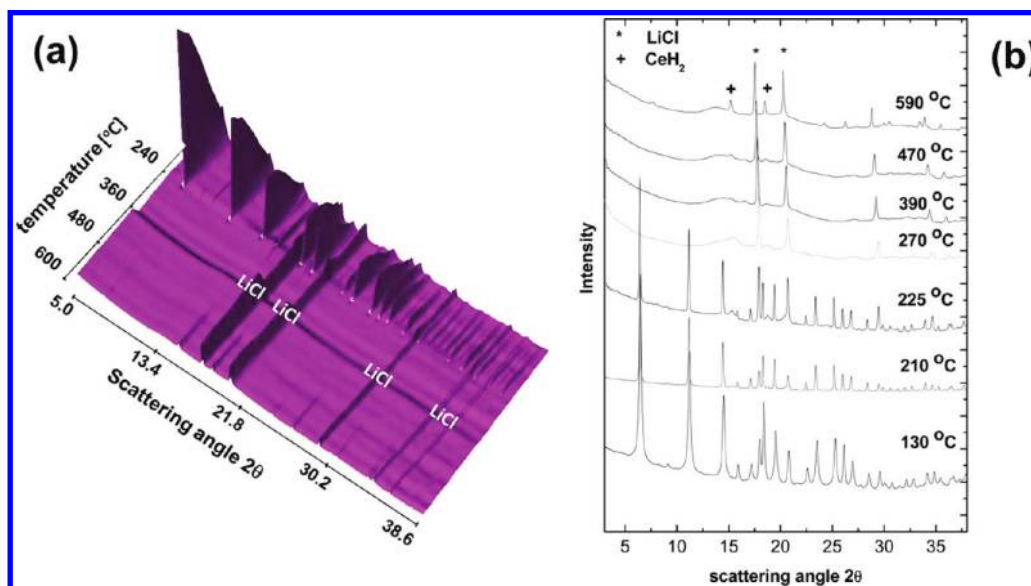


Figure 9. (a) In situ SR-PXD data obtained in the temperature region between 80 and 600 °C. (b) Selected powder patterns between 130 and 590 °C. The heating rate was 2 °C/min. Peak positions of the major phases have been indicated in the plots.

distinct peaks are observed at 261 and 302 °C, and in addition a shoulder at 289 °C in between those peaks is visible. The peak position of the final endothermic event at each heating rate was used to calculate the activation energy for the thermal decomposition according to the Kissinger equation

$$\frac{d \left[\ln \left(\frac{\beta}{T_p^2} \right) \right]}{d \left(\frac{1}{T} \right)} = \frac{E_a}{R} \quad (6)$$

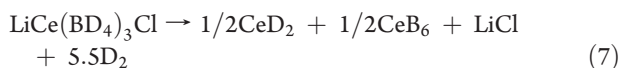
where β and E_a denote the heating rate and activation energy, T is the peak temperature, and R represents the molar gas constant. The result of this calculation is presented in Figure 8b, where the slope of the straight line corresponds to the activation energy for the decomposition (taken from the last desorption peak). The

value of 106(6) kJ/mol is considerably smaller than that for the bulk of LiBH_4 with additives.^{3,46} It is also >20% smaller than the 136(6) kJ/mol that was obtained by Gennari et al. for ball-milled mixtures of $3\text{LiBH}_4\text{-CeCl}_3$.¹⁹ It demonstrates that the interaction between LiBH_4 and CeCl_3 reduces the kinetic barriers for hydrogen desorption very effectively.

To study the thermal decomposition in detail and to obtain information about decomposition products and possible intermediates, in situ SR-PXD experiments were conducted at SNBL. Figure 9a shows the evolution of powder patterns as a function of temperature between 80 and 600 °C, whereas Figure 9b displays powder patterns at selected temperatures in more detail. The experiments were performed with a constant heating rate of 2 °C/min under dynamic vacuum for a ($3\text{LiBD}_4\text{-CeCl}_3$) mixture obtained after ball-milling (6 h). In the low-temperature region

between 80 and 150 °C, the X-ray profiles become narrower and the overall intensity of the peaks increases (Figure 9a). This indicates that the crystallinity of the material increases during annealing. A similar finding was made by ex situ post annealing of a ball-milled mixture under deuterium back pressure. The only crystalline phases present after ball-milling are LiCl and LiCe(BD₄)₃Cl, respectively, and the latter is stable up to its decomposition temperature of ~240 °C (Figure 9a). At this temperature, peaks belonging to this phase vanish and the SR-PXD pattern exhibits only peaks belonging to LiCl. Going to higher temperatures, between 270 and 450 °C, the data exhibit a broad and featureless region around $2\theta = 15^\circ$. This is characteristic of some amorphous boron containing compounds in addition to LiCl, which could either be boron itself or a Ce–B containing species. Above 450 °C, new peaks start to appear, sharpen up, and gain in intensity up to the final temperature of 600 °C. They have been assigned to cerium hydride, CeH₂, and are highlighted in Figure 9b.

Taking these findings into account the thermal decomposition could proceed via the following alternative pathways



or



Reaction 7 would liberate ~6.8 wt % with respect to the total mass of the 3LiBD₄–CeCl₃ starting mixture, whereas reaction 8 releases only ~6.2 wt %.

In three recent papers, the thermal decomposition of LiBH₄–CeCl₃ mixtures in different ratios has been studied, and the results are presented based on the assumption that Ce(BH₄)₃ is the material that undergoes the dehydrogenation. All authors propose decomposition pathways similar to eqs 7 and 8, in which the decomposition products are both cerium hydride and boron or cerium hydride and cerium boride. In the first of this series, Gennari et al.¹⁹ find the presence of CeH₂ after heating a sample ex situ to 350 °C for a period of 1 day. Although they did not observe CeB₆ directly by XRD, they postulate its formation because their measured gas release is more consistent with its presence rather than the formation of amorphous boron. In addition, they provide thermodynamic considerations that favor the formation of CeB₆ instead of boron. Liu et al.²⁰ dehydrogenated a 3LiBH₄–CeCl₃ mixture up to 600 °C and studied the decomposition products ex situ by XRD. They obtained crystalline CeB₆ after heating the mixture up to 600 °C for an extended period of time. In the last Article, Gennari et al.⁴⁷ study the reversible hydrogen storage from 6LiBH₄–MCl₃ (M = Ce, Gd) mixtures and find that the MH₂ species initially formed during dehydrogenation interact with the excess LiBH₄, thereby destabilizing LiBH₄, leading to a decrease in dehydrogenation temperature compared with as-milled LiBH₄. They identify the primary dehydrogenation products as CeB₆–LiH and Gd₂B₄–LiH, respectively.

From these findings, the formation of CeB₆ seems plausible, at least at high temperatures and extended times. The fact that we did not observe CeB₆ during our in situ SR-PXD studies is not contradicting because the time was basically too short to allow it to appear as a crystalline phase. Also, the fact that we observe slightly less gas release (6.2 wt %) during the TG-DSC experiment up to 400 °C compared with the theoretical value of

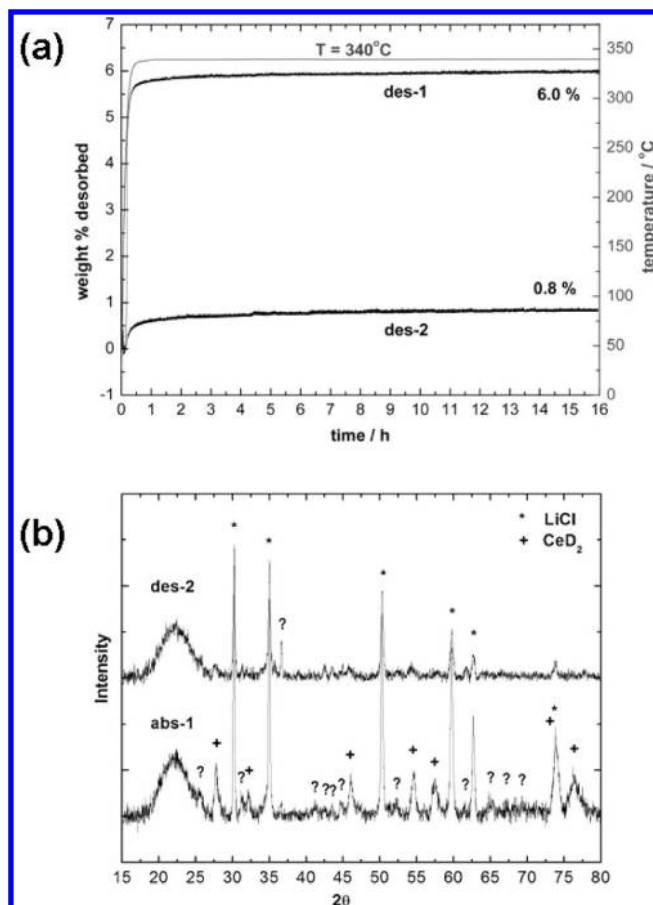


Figure 10. (a) Volumetric gas release during the first and second dehydrogenation cycle for a ball-milled mixture of LiBD₄–CeCl₃ (3:1 ratio) at $T = 340^\circ\text{C}$. (b) Ex situ X-ray powder patterns obtained after rehydrogenation (abs-1) and subsequent dehydrogenation (des-2) at 340°C .

6.8 wt % does not eliminate the possibility for the formation of CeB₆. It could simply indicate that this particular material is not yet fully decomposed, that it is not fully deuterated, or that part of its deuterium content is still trapped, maybe in form of an amorphous Ce–B–D containing intermediate. Note that we also performed an additional TG “control experiment” (not shown) on a 3LiBH₄–CeCl₃ hydride mixture after ball-milling (6 h) for which we found a weight loss of 3.5 wt % with respect to the starting mixture. This value is in excellent agreement with the expected weight loss of 3.6 wt % assuming the formation of CeH₂ and CeB₆ in eq 7.

Rehydrogenation Properties. To explore the reversibility of the ball-milled 3LiBD₄–CeCl₃ mixture, dehydrogenation, and rehydrogenation experiments were carried out in a Sieverts-type apparatus. The sample was first heated to 340 °C at a rate of 9 °C/min under vacuum (10^{-3} bar) and kept at this temperature for a period of 16 h. It released ~6 wt % of gas during the first dehydrogenation. (See Figure 10a.) After rehydrogenating at 340 °C under 80 bar of deuterium for a period of 24 h, a second dehydrogenation procedure was performed again at 340 °C under vacuum. The accumulated gas release after the second dehydrogenation was 0.8 wt %. (See Figure 10a.) This amount attributes to ~13% of the initial gas release obtained after the first dehydrogenation and demonstrates that the system is only partially reversible at best.

PXD patterns (Figure 10b) were recorded to elucidate the nature of the decomposition products and to identify the origin for the partial reversibility. After the first rehydrogenation (abs-1), the powder pattern shows peaks associated with LiCl and CeD₂ as majority phases. Their corresponding peak positions have been highlighted in Figure 10b. A broad and featureless bump is also visible between $2\theta = 20$ and 25° that can be attributed to amorphous boron containing species. It either may have its origin in the boron-containing glass-capillary that was used as a sample holder or may be due to amorphous Ce–B-containing species that were formed prior during decomposition. The PXD pattern after the second dehydrogenation step (des-2) exhibits mainly peaks associated with the presence of LiCl and minor contributions from CeD₂. The intensity of the peaks associated with CeD₂ is less than that found after the first rehydrogenation.

In addition to LiCl and CeD₂, there are weak peaks visible in the pattern, which have been indicated by a question mark (Figure 10b). They belong neither to any kind of Ce–B or Ce–D species nor to any oxygen-containing phases that may have formed due to contamination. The fact that the intensity of these peaks is larger than after the second dehydrogenation step (des-2) indicates that they could belong to an intermediate phase that forms during rehydrogenation and that accounts for the partial reversibility of the system.

The existence of an intermediate phase has already been postulated by Zhang et al.²⁰ during their rehydrogenation investigations of LiBH₄–LnX₃ mixtures (Ln = Ce, La; X = Cl, F) but the authors were unable to determine their exact nature. We find a strong resemblance between the intermediate phase observed in our PXD data with their unidentified decomposition products obtained from the decomposition of Ce(BH₄)₃. In our case the material that undergoes decomposition, however, is not Ce(BH₄)₃ but rather the mixed-metal and anion-substituted compound LiCe(BD₄)₃Cl.

It seems likely that Ce–B–H containing species, for example, cluster-like compounds like Ce(B₁₂H₁₂)₃ or other boranes, are formed during the decomposition of the samples by analogy to those found in other borohydrides like LiBH₄, LiSc(BH₄)₄,⁴⁸ and Mg(BH₄)₂.⁴⁹ Their structural characterization remains challenging, however, because of their low abundance and low crystallinity in the present study.

To make the LiBH₄–CeCl₃ system more attractive as hydrogen-storage material, the reversibility for the rehydrogenation needs to be drastically improved. Gennari et al.⁴⁷ have recently demonstrated that the stoichiometry of the initial mixture has an influence on the reversibility and the nature of the decomposition products. They observed that ball-milled mixtures of LiBH₄–CeCl₃ in a molar ratio of 6:1 lead to a destabilization of the excess LiBH₄ by in situ formed CeH₂. The dehydrogenation products in this case were mainly CeB₆ and LiH, which could be rehydrogenated to a greater extent under moderate conditions, for example, 400 °C and 60 bar of hydrogen.

This is an encouraging result and leaves room for further developments and alternate approaches, for example, the use of an additional catalyst that improves the rehydrogenation properties and reversibility of the intermediate phases that are formed during the decomposition of LiBH₄–CeCl₃ mixtures in various ratios.

CONCLUSIONS

The mechanochemical reaction between LiBH₄ and CeCl₃ in a molar ratio of 3:1 has led to the formation of the first

mixed-metal and anion-substituted rare earth borohydride LiCe(BH₄)₃Cl. The material crystallizes in the cubic space group $\bar{I}43m$ with $a = 11.5916(1)$ Å. There is good agreement between the parameters obtained from the structural optimization using DFT calculations and the experimental study. Partial DOS and charge density analysis predicts that LiCe(BH₄)₃Cl has the characteristics of an insulator. The bonds between Li, Cl, Ce and the host lattice are found to be ionic. However, the bonding interaction between B and H is mixed ionic-covalent.

LiCe(BH₄)₃Cl decomposes above 220 °C into CeH₂ and amorphous boron-containing species. The decomposition temperature is considerably lower than that of pure LiBH₄, which demonstrates that CeCl₃ is a very effective destabilization agent for LiBH₄. The material shows partial reversibility and reabsorbs ~13 wt % of its original hydrogen content at 340 °C and 80 bar of hydrogen.

ASSOCIATED CONTENT

S Supporting Information. Crystallographic information files and a full list of the calculated IR/Raman frequencies. This material is available free of charge via the Internet at <http://pubs.acs.org>.

AUTHOR INFORMATION

Corresponding Author

*Phone: +47 6380 6444. Fax: +47 6380 6388. E-mail: christoph.frommen@ife.no.

ACKNOWLEDGMENT

The NANOMAT and RENERGI programs of the Research Council of Norway are gratefully acknowledged for their financial support. The skillful assistance from the project team at the Beamlines BM01A and BM01B, ESRF, Grenoble, is also gratefully acknowledged.

REFERENCES

- (1) Schlapbach, L.; Züttel, A. *Nature* **2001**, *414*, 353.
- (2) Orimo, S. I.; Nakamori, Y.; Eliseo, J. R.; Züttel, A.; Jensen, C. M. *Chem. Rev.* **2007**, *107*, 4111.
- (3) Züttel, A.; Wenger, P.; Rentsch, S.; Sudan, P.; Mauron, P.; Emmenegger, C. *J. Power Sources* **2003**, *118*, 1.
- (4) Nickels, E. A.; Jones, M. O.; David, W. I. F.; Johnson, S. R.; Lowton, R. L.; Sommariva, M.; Edwards, P. P. *Angew. Chem., Int. Ed.* **2008**, *47*, 2817.
- (5) Hagemann, H.; Longhini, M.; Kaminski, J. W.; Wesolowski, T. A.; Cerny, R.; Penin, N.; Sorby, M. H.; Hauback, B. C.; Severa, G.; Jensen, C. M. *J. Phys. Chem. A* **2008**, *112*, 7551.
- (6) Kim, C.; Hwang, S. J.; Bowman, R. C.; Reiter, J. W.; Zan, J. A.; Kulleck, J. G.; Kabbour, H.; Majzoub, E. H.; Ozolins, V. *J. Phys. Chem. C* **2009**, *113*, 9956.
- (7) Cerny, R.; Severa, G.; Ravnsbaek, D. B.; Filinchuk, Y.; D'Anna, V.; Hagemann, H.; Haase, D.; Jensen, C. M.; Jensen, T. R. *J. Phys. Chem. C* **2010**, *114*, 1357.
- (8) Cerny, R.; Ravnsbaek, D. B.; Severa, G.; Filinchuk, Y.; D'Anna, V.; Hagemann, H.; Haase, D.; Skibsted, J.; Jensen, C. M.; Jensen, T. R. *J. Phys. Chem. C* **2010**, *114*, 19540.
- (9) Ravnsbaek, D.; Filinchuk, Y.; Cerenius, Y.; Jakobsen, H. J.; Besenbacher, F.; Skibsted, J.; Jensen, T. R. *Angew. Chem., Int. Ed.* **2009**, *48*, 6659.
- (10) Cerny, R.; Penin, N.; Hagemann, H.; Filinchuk, Y. *J. Phys. Chem. C* **2009**, *113*, 9003.

- (11) Sato, T.; Miwa, K.; Nakamori, Y.; Ohoyama, K.; Li, H. W.; Noritake, T.; Aoki, M.; Towata, S. I.; Orimo, S. I. *Phys. Rev. B* **2008**, *77*, 104114.
- (12) Frommen, C.; Aliouane, N.; Deledda, S.; Fonnelop, J. E.; Grove, H.; Lieutenant, K.; Llamas-Jansa, I.; Sartori, S.; Sorby, M. H.; Hauback, B. C. *J. Alloys Compd.* **2010**, *496*, 710.
- (13) Ravnsbæk, D. B.; Filinchuk, Y.; Cerny, R.; Ley, M. B.; Haase, D. r.; Jakobsen, H. J.; Skibsted, J. r.; Jensen, T. R. *Inorg. Chem.* **2010**, *49*, 3801.
- (14) Yan, Y. G.; Li, H. W.; Sato, T.; Umeda, N.; Miwa, K.; Towata, S.; Orimo, S. *Int. J. Hydrogen Energy* **2009**, *34*, 5732.
- (15) Jaron, T.; Grochala, W. *Dalton Trans.* **2010**, *39*, 160.
- (16) Lee, Y. S.; Shim, J. H.; Cho, Y. W. *J. Phys. Chem. C* **2010**, *114*, 12833.
- (17) Andrade-Gamboa, J.; Puzkiel, J. A.; Fernandez-Albanesi, L.; Gennari, F. C. *Int. J. Hydrogen Energy* **2010**, *35*, 10324.
- (18) Ravnsbaek, D. B.; Sorensen, L. H.; Filinchuk, Y.; Reed, D.; Book, D.; Jakobsen, H. J.; Besenbacher, F.; Skibsted, J.; Jensen, T. R. *Eur. J. Inorg. Chem.* **2010**, 1608.
- (19) Gennari, F. C.; Esquivel, M. R. *J. Alloys Compd.* **2009**, *485*, L47.
- (20) Zhang, B. J.; Liu, B. H.; Li, Z. P. *J. Alloys Compd.* **2011**, *509*, 751.
- (21) Hauback, B. C.; Fjellvåg, H.; Steinsvoll, O.; Johansson, K.; Buset, O. T.; Jørgensen, J. *J. Neutron Res.* **2000**, *8*, 215.
- (22) Favre-Nicolin, V.; Cerny, R. *J. Appl. Crystallogr.* **2002**, *35*, 734.
- (23) Favre-Nicolin, V.; Cerny, R. *Z. Kristallogr.* **2004**, *219*, 847.
- (24) Rodriguez-Carvajal, J. *Physica B* **1993**, *192*, 55.
- (25) Hammersley, A. P. *IT2D: An Introduction and Overview*; ESRF Internal Report ESRF97HA02T; ESRF: Grenoble, France, 1997.
- (26) Kresse, G.; Hafner, J. *Phys. Rev. B* **1993**, *47*, 558.
- (27) Blochl, P. E. *Phys. Rev. B* **1994**, *50*, 17953.
- (28) Kresse, G.; Joubert, D. *Phys. Rev. B* **1999**, *59*, 1758.
- (29) Kohn, W.; Sham, L. J. *Phys. Rev.* **1965**, *136*.
- (30) Payne, M. C.; Teter, M. P.; Allan, D. C.; Arias, T. A.; Joannopoulos, J. D. *Rev. Mod. Phys.* **1992**, *64*, 1045.
- (31) Pulay, P. *Chem. Phys. Lett.* **1980**, *73*, 393.
- (32) Perdew, J. P.; Ruzsinszky, A.; Csonka, G. I.; Vydrov, O. A.; Scuseria, G. E.; Constantin, L. A.; Zhou, X. L.; Burke, K. *Phys. Rev. Lett.* **2008**, *100*.
- (33) Perdew, J. P.; Ruzsinszky, A.; Csonka, G. I.; Vydrov, O. A.; Scuseria, G. E.; Constantin, L. A.; Zhou, X. L.; Burke, K. *Phys. Rev. Lett.* **2009**, *102*.
- (34) Csonka, G. I.; Perdew, J. P.; Ruzsinszky, A.; Philipsen, P. H. T.; Lebegue, S.; Paier, J.; Vydrov, O. A.; Angyan, J. G. *Phys. Rev. B* **2009**, *79*, 155107.
- (35) Boulitf, A.; Louer, D. *J. Appl. Crystallogr.* **1991**, *24*, 987.
- (36) Laugier, J.; Bochu, B. *LMGP-Suite of Programs for the Interpretation of X-ray Experiments*; ENSP/Laboratoire des Matériaux et du Génie Physique: Saint Martin d'Hères, France.
- (37) Acevedo, R.; Poblete, V. *Powder Diffr.* **1995**, *10*, 241.
- (38) Seifert, H. J. *Therm. Anal. Calorim.* **2002**, *67*, 789.
- (39) Chakoumakos, B. C.; Custelcean, R.; Ramey, J. O.; Kolopus, J. A.; Jin, R. Y.; Neal, J. S.; Wisniewski, D. J.; Boatner, L. A. *Cryst. Growth Des.* **2008**, *8*, 2070.
- (40) Zachariasen, W. *Acta Crystallogr.* **1948**, *1*, 265.
- (41) Shannon, R. D. *Acta Crystallogr., Sect. A* **1976**, *32*, 751.
- (42) Harvey, K. B.; McQuaker, N. R. *Can. J. Chem.* **1971**, *49*, 3282.
- (43) Racu, A. M.; Schoenes, J.; Lodziana, Z.; Borgschulte, A.; Zuttel, A. *J. Phys. Chem. A* **2008**, *112*, 9716.
- (44) Clark, S. J.; Segall, M. D.; Pickard, C. J.; Hasnip, P. J.; Probert, M. I. J.; Refson, K.; Payne, M. C. *Z. Kristallogr.* **2005**, *220*, 567.
- (45) Nakamori, Y.; Li, H. W.; Kikuchi, K.; Aoki, M.; Miwa, K.; Towata, S.; Orimo, S. *J. Alloys Compd.* **2007**, *296*, 446–447.
- (46) Zhang, Y.; Zhang, W. S.; Wang, A. Q.; Sun, L. X.; Fan, M. Q.; Chu, H. L.; Sun, J. C.; Zhang, T. *Int. J. Hydrogen Energy* **2007**, *32*, 3976.
- (47) Gennari, F. C.; Albanesi, L. F.; Puzkiel, J. A.; Larochette, P. A. *Int. J. Hydrogen Energy* **2011**, *36*, 563.
- (48) Hwang, S. J.; Bowman, R. C.; Reiter, J. W.; Rijssenbeek, J.; Soloveichik, G. L.; Zhao, J. C.; Kabbour, H.; Ahn, C. C. *J. Phys. Chem. C* **2008**, *112*, 3164.
- (49) Soloveichik, G. L.; Gao, Y.; Rijssenbeek, J.; Andrus, M.; Kniajanski, S.; Bowman, R. C.; Hwan, S. J.; Zhao, J. C. *Int. J. Hydrogen Energy* **2009**, *34*, 916.